Article

Scaling of the strange-metal scattering in unconventional superconductors

https://doi.org/10.1038/s41586-021-04305-5

Received: 30 March 2021

Accepted: 29 November 2021

Published online: 16 February 2022

Check for updates

Jie Yuan[1,2,8], Qihong Chen[1,3,8], Kun Jiang[1], Zhongpei Feng[1,3], Zefeng Lin[1], Heshan Yu[1], Ge He[1], Jinsong Zhang[1], Xingyu Jiang[1], Xu Zhang[1], Yujun Shi[1], Yanmin Zhang[1], Mingyang Qin[1], Zhi Gang Cheng[1,3], Nobumichi Tamura[4], Yi-feng Yang[1], Tao Xiang[1,5], Jiangping Hu[1,3]✉, Ichiro Takeuchi[6,7]✉, Kui Jin[1,2,3]✉ & Zhongxian Zhao[1,2,3]

Marked evolution of properties with minute changes in the doping level is a hallmark of the complex chemistry that governs copper oxide superconductivity as manifested in the celebrated superconducting domes and quantum criticality taking place at precise compositions[1–4]. The strange-metal state, in which the resistivity varies linearly with temperature, has emerged as a central feature in the normal state of copper oxide superconductors[5–9]. The ubiquity of this behaviour signals an intimate link between the scattering mechanism and superconductivity[10–12]. However, a clear quantitative picture of the correlation has been lacking. Here we report the observation of precise quantitative scaling laws among the superconducting transition temperature (T_c), the linear-in-T scattering coefficient (A_1) and the doping level (x) in electron-doped copper oxide $La_{2-x}Ce_xCuO_4$ (LCCO). High-resolution characterization of epitaxial composition-spread films, which encompass the entire overdoped range of LCCO, has enabled us to systematically map its structural and transport properties with unprecedented accuracy and with increments of $\Delta x = 0.0015$. We have uncovered the relations $T_c \sim (x_c - x)^{0.5} \sim (A_1^{\square})^{0.5}$, where x_c is the critical doping in which superconductivity disappears and $A_1^{\square}$ is the coefficient of the linear resistivity per CuO_2 plane. The striking similarity of the T_c versus $A_1^{\square}$ relation among copper oxides, iron-based and organic superconductors may be an indication of a common mechanism of the strange-metal behaviour and unconventional superconductivity in these systems.

The strange-metal behaviour in the normal-state resistivity of copper oxide superconductors was first observed shortly after their discovery. The unusual behaviour in which the resistivity varies as a linear function of temperature (linear-in-T resistivity) up to several hundred kelvin has now been reported in several superconducting copper oxides[5,6]. In a narrow composition region around optimal doping, the linear-in-T behaviour extends to low temperatures (close to T_c)[6], indicating a critical behaviour at the quantum critical point (QCP). In a hole-doped copper oxide $La_{2-x}Sr_xCuO_4$ (LSCO), the linear-in-T resistivity was found to dominate the normal-state transport down to 1.5 K in an extended range near the optimal doping, with superconductivity suppressed by high magnetic fields[7]. For electron-doped copper oxides, a perfect linear-in-T resistivity persists down to 40 mK in $Pr_{2-x}Ce_xCuO_4$ (ref. [8]) and to 20 mK in $La_{2-x}Ce_xCuO_4$ (LCCO)[9]. In particular, the strange-metal behaviour in LCCO was found to start at the doping level associated with the Fermi surface reconstruction ($x \approx 0.14$) to the endpoint of the superconducting dome ($x_c \approx 0.175 \pm 0.005$), where it enters a metallic (non-superconducting) Fermi-liquid state[11]. Very recently the strange-metal state has also been observed in the antiferromagnetic (AF) regime (for example, $x = 0.12$ and 0.13)[13]. An important feature of the strange-metal state is that the coefficient of linear-in-T resistivity (that is, A_1 from $\rho = \rho_0 + A_1 T$) shows a positive correlation with T_c, suggesting an intimate link between the anomalous normal state and the superconductivity[9,10].

There has been a concerted effort in the community to quantify the relationship between A_1 and T_c as a direct function of the chemical doping concentration[10,11]. However, owing to the lack of sufficient data points with enough density to map across the doping phase diagrams, an explicit expression had been unknown. To this end, we have used high-precision thin-film composition spreads encompassing the entire overdoped range of LCCO with incremental accuracy in doping concentration Δx of 0.0015. The systematic measurements have uncovered a notable scaling law linking the superconducting transition temperature (T_c), doping level (x) and the T-linear coefficient ($A_1^{\square}$), namely $T_c \sim (x_c - x)^{0.5} \sim (A_1^{\square})^{0.5}$. Here $A_1^{\square}$ is the T-linear coefficient normalized by the distance between adjacent CuO_2 planes, that is, $A_1^{\square} = A_1/d$, where d is half of the c-axis lattice constant ($d = c/2$), mapped accurately across the spread. Our findings perhaps point to a universal relation between

[1]Beijing National Laboratory for Condensed Matter Physics, Institute of Physics, Chinese Academy of Sciences, Beijing, China. [2]Key Laboratory of Vacuum Physics, School of Physical Sciences, University of Chinese Academy of Sciences, Beijing, China. [3]Songshan Lake Materials Laboratory, Dongguan, Guangdong, China. [4]Advanced Light Source, Lawrence Berkeley National Laboratory, Berkeley, CA, USA. [5]Beijing Academy of Quantum Information Sciences, Beijing, China. [6]Department of Materials Science and Engineering, University of Maryland, College Park, MD, USA. [7]Maryland Quantum Materials Center, Department of Physics, University of Maryland, College Park, MD, USA. [8]These authors contributed equally: Jie Yuan, Qihong Chen
✉e-mail: jphu@iphy.ac.cn; takeuchi@umd.edu; kuijin@iphy.ac.cn

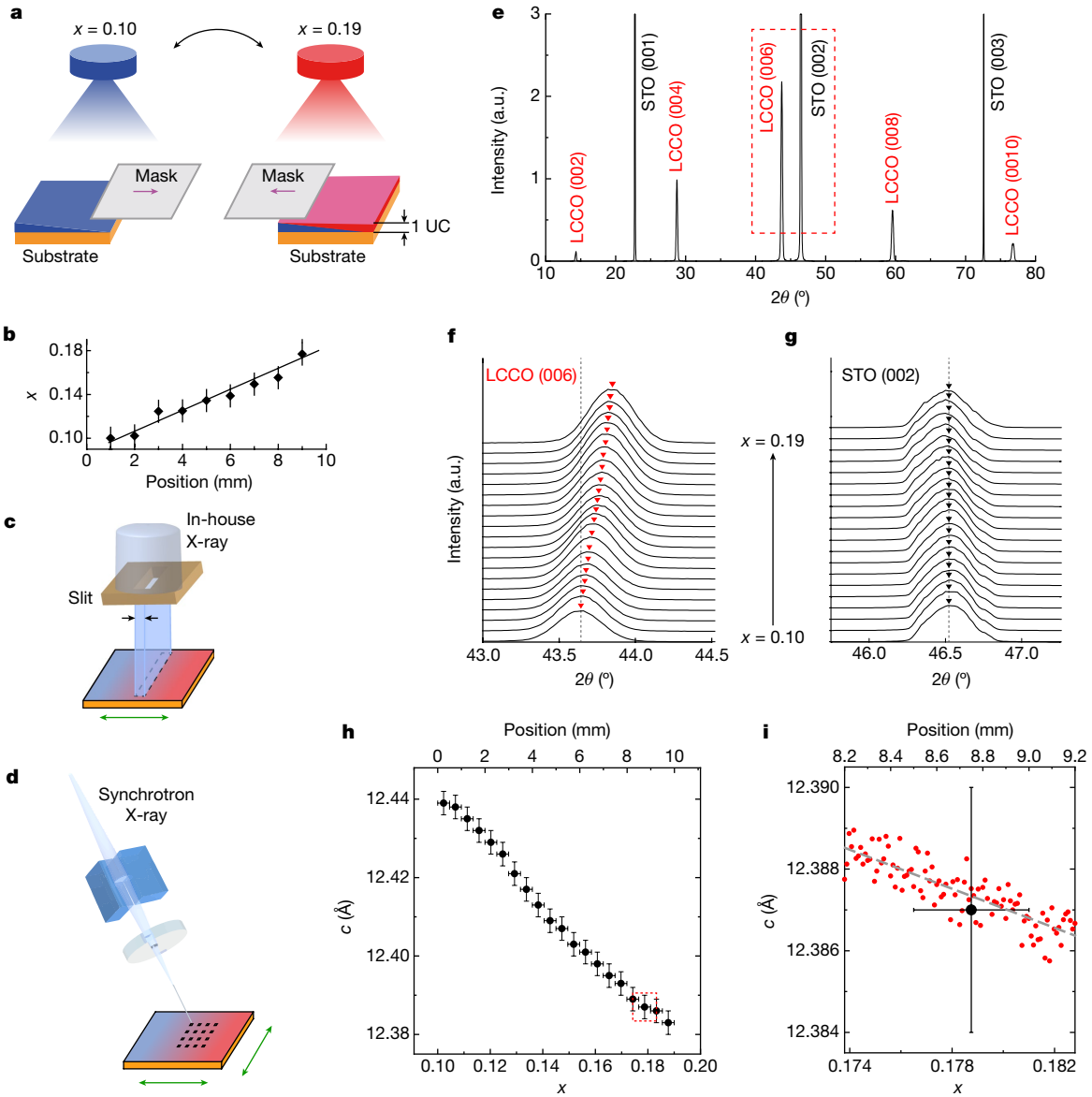

Fig. 1 | Combinatorial synthesis and multiscale structural characterization of LCCO. a, Schematic illustration of the composition-spread epitaxial growth of LCCO on a STO substrate. Two targets with end compositions of the spread are ablated alternately, during which a shadow mask moves in such a way to create unit-cell-thick linear deposition gradients in opposite directions. The total thickness of the film (uniform across the spread) can be controlled by the number of gradient pairs to be deposited. UC, unit cell. **b**, The Ce doping level mapped across a spread with WDS. The error bars reflect the uncertainty in the WDS measurement. **c**, **d**, Schematic illustrations of the in-house (**c**) and synchrotron (**d**) XRD measurement configurations, with beam width of 0.4 mm and spot size of 1 μm^2, respectively. **e**, The $\theta/2\theta$ XRD pattern obtained by the in-house diffractometer. a.u., arbitrary units. **f**, **g**, The individual XRD patterns of the magnified 2θ region (dashed box region in **e**), showing the LCCO (006) (**f**) and STO (002) (**g**) Bragg peaks. The lines from different compositions (0.5 mm step) are vertically shifted for clarity. The vertical dashed lines are guides to discern the peak shift. The inverted triangles mark the peak positions of each line. **h**, The doping dependence of the *c*-axis lattice constant across the spread measured by the in-house XRD setup. The horizontal and vertical error bars reflect the uncertainty from the width of the X-ray beam and the accuracy of the diffractometer, respectively. **i**, The doping dependence of the *c*-axis lattice constant obtained by synchrotron XRD (red) corresponding to the region depicted by the dashed box in **h**. One lattice constant measurement (and error bars) obtained in this range in **h** is shown for comparison (black). The grey dashed line is the linear fit for estimation of the uncertainty.

the normalized *T*-linear coefficient and T_c among copper oxides, pnictides and a class of organic superconductors, strongly suggestive of a common underlying physics at work in these unconventional superconductors.

Because of the relatively complex synthesis process, it has been non-trivial to tune the composition of LCCO films with high precision. We overturn this challenge by using combinatorial laser molecular beam epitaxy[14,15] combined with micrometre-scale systematic characterization. The synthesis scheme is shown in Fig. 1a. Two targets with nominal compositions of $La_{1.90}Ce_{0.10}CuO_4$ and $La_{1.81}Ce_{0.19}CuO_4$ are used as two ends of the composition spreads, corresponding to the optimal doping ($x = 0.10$) with the highest T_c and the metallic Fermi-liquid state ($x = 0.19$), respectively. A series of unit-cell-thick gradient wedges are deposited using the two targets in an alternating manner using moving mechanical shutters at 700 °C on a $SrTiO_3$ (STO) (100) substrate. This results in a *c*-axis-oriented epitaxial composition-spread LCCO thin film with continuously varying composition between $La_{1.90}Ce_{0.10}CuO_4$ and $La_{1.81}Ce_{0.19}CuO_4$ with uniform total thickness across the 10 mm length of the substrate. This growth technique ensures that the synthesis conditions are identical for the entire doping range.

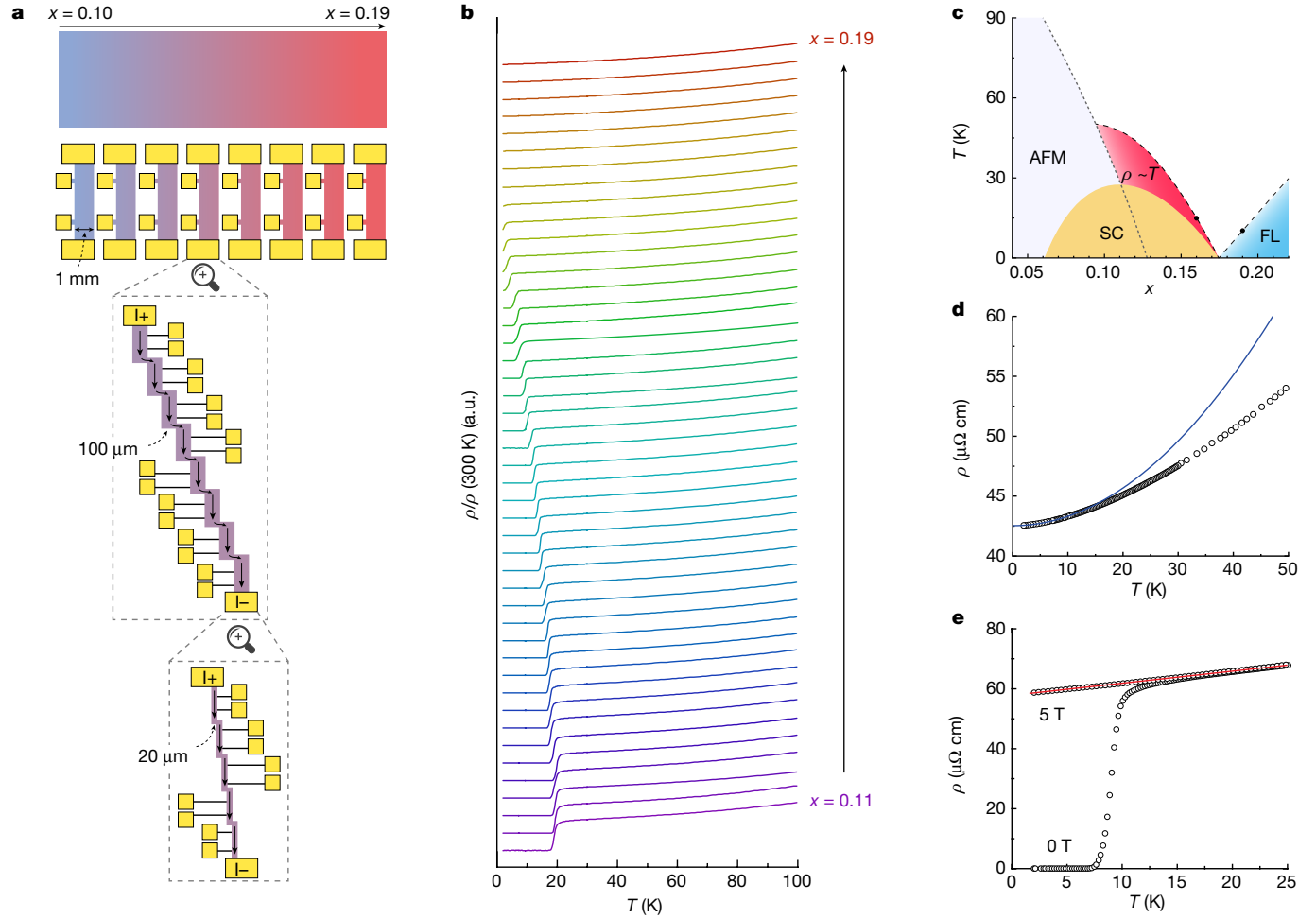

Fig. 2 | Microregion characterizations of electrical transport properties. **a**, Configurations of the patterned bridges for transport measurements across the spread. There are three levels of pattern arrays with successively decreasing microbridge widths: 1 mm, 100 µm and 20 µm from the widest to the narrowest. In this way, the spatial resolution of the transport measurement can reach the length scale comparable to the synchrotron microdiffraction mapping. **b**, Temperature dependence of the resistivity $\rho(T)$ for 100-µm-wide bridges patterned across the spread. The resistivity is normalized by its value at 300 K, and the curves are vertically shifted for comparison. **c**, The phase diagram of LCCO. AFM, antiferromagnetism; SC, superconductivity; FL, Fermi liquid. Two representative dopings $x = 0.16$ and $x = 0.19$ are chosen for demonstration of the strange-metal and Fermi liquid behaviour, respectively. **d**, Temperature dependence of the resistivity for $x = 0.19$. The solid line is the fit using the Fermi liquid formula: $\rho = \rho_0 + A_2T^2$. **e**, Temperature dependence of the resistivity for a bridge ($x = 0.16$) with $T_c \sim 10$ K at $B = 0$ T, and with a magnetic field of $B = 5$ T applied perpendicular to the film. The red straight line is a linear fit with $\rho = \rho_0 + A_1T$.

We first perform standard 'low resolution' analysis of the composition and the corresponding *c*-axis lattice constant variation across the spread using wavelength-dispersive X-ray spectroscopy (WDS) and an in-house diffractometer, respectively. As shown in Fig. 1b, the WDS-mapped cerium (Ce) concentration in the LCCO film shows the expected dependence on position, spanning $0.10 \leq x \leq 0.19$. The uncertainty in the determined concentration from WDS is typically 2%. Figure 1e shows the $\theta/2\theta$ X-ray diffraction (XRD) pattern from the entire spread integrated along the direction of compositional gradient. Figure 1f, g shows the LCCO (006) and STO (002) peaks, respectively, mapped at different positions along the spread using the in-house diffractometer with a beam size of 0.4 mm (Fig. 1c) and steps of 0.5 mm. The LCCO (006) peak moves to higher angles as the doping concentration is increased, whereas the STO (002) peak does not change. Figure 1h shows the corresponding lattice constant mapping across the spread chip with error bars determined by limitations of the beam size of the in-house diffractometer operated under standard conditions. The smooth and well-behaved overall variation of the composition and the lattice constant over the entire length of the spread is therefore confirmed despite relatively large measurement uncertainties associated with in-house characterization.

To harness the wealth of information that resides in the epitaxial spread at high spatial resolution, we enlist synchrotron microbeam diffraction (Fig. 1d) whose 1 µm^2 beam spot size (together with micrometre-level accuracy of its scanning stage) allows the ultimate determination of the composition variation sensitivity and the smallest meaningful increment with which we can extract composition-dependent properties from the spread. Figure 1i shows the lattice constant mapping obtained from a part of the spread using the microbeam with 10 µm position increment across the spread (taken at Beamline 12.3.2 at Advanced Light Source). The variation of the lattice constant from point to point as well as its linear regression indicates that it can be determined with an uncertainty of 0.001 Å, which corresponds to the compositional variation Δx of 0.0015. We note that such accuracy in composition control is not possible with traditional chemical synthesis methods[9]. As positions on the spread can be readily specified with accuracy down to micrometres, these numbers ensure that we can obtain statistically significant mapping of composition-dependent properties with high incremental density in the 10 mm length of the spread encompassing $\Delta x \approx 0.09$.

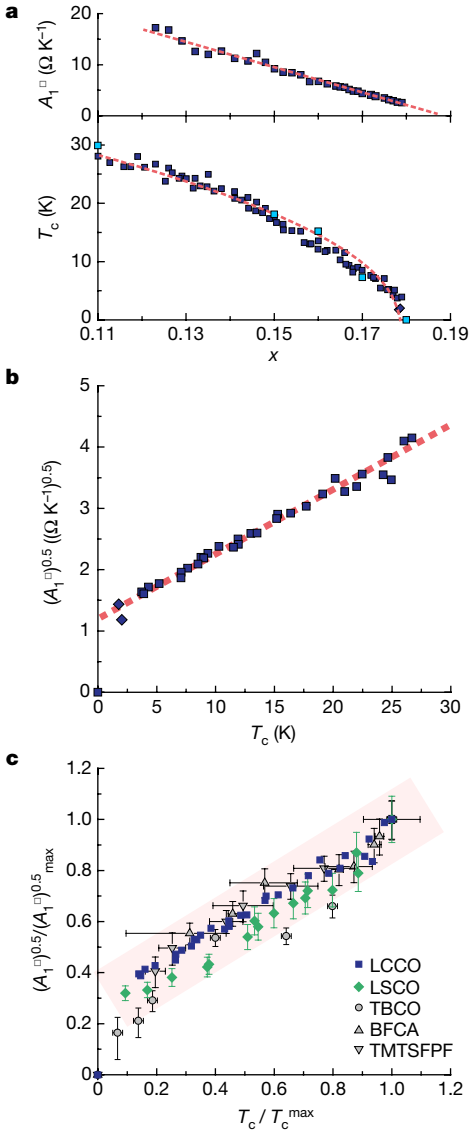

Fig. 3 | Quantitative scaling revealed from the systematic spread data and comparison of different unconventional superconductors. a, Doping dependence of T_c (bottom) and $A_1^{\square}$ (top). Across the full spread-film doping range, T_c exhibits a square root dependence on doping, $T_c \propto (x_c - x)^{0.5}$, whereas $A_1^{\square}$ shows a clear linear dependence on doping. The T_c data are collected from two composition-spread films. The light blue squares are extracted from ref. [9]. **b**, $(A_1^{\square})^{0.5}$ as a function of T_c extracted from the $\rho(T)$ curves (Extended Data Fig. 1 and Extended Data Table 1). The diamonds at low T_c values are extracted from two bridges with temperature measured to a few hundred millikelvin. The dashed line shows the linear fit. **c**, The correlation between $(A_1^{\square})^{0.5}$ and T_c for different superconducting systems from the literature, with $(A_1^{\square})^{0.5}$ and T_c normalized by their respective maximum values. TBCO, $Tl_2Ba_2CuO_{6+\delta}$; TMTSFPF, $(TMTSF)_2PF_6$; BFCA, $Ba(Fe_{1-x}Co_x)_2As_2$. LSCO data are extracted from the $\rho(T)$ curves in ref. [20]; data for $(TMTSF)_2PF_6$, $Tl_2Ba_2CuO_{6+\delta}$ and $Ba(Fe_{1-x}Co_x)_2As_2$ are from ref. [10] and references therein. The error bars are reproduced from published data and reflect the uncertainty in determining T_c and the T-linear coefficient.

The transport properties are obtained by patterning the spread film into microbridge arrays, as schematically shown in Fig. 2a. Initially, the entire LCCO spread film is patterned into eight bridges, each with a width of 1 mm, for rapidly surveying the superconducting properties over the spread. Each bridge is then divided into eight smaller bridges, each with a width of 100 μm. At the last step, some bridges with compositions near where the superconductivity disappears have been patterned into 20-μm-wide bridges to study the delicate critical behaviour.

The $\rho(T)$ (temperature dependence of resistivity) data obtained from all 100 μm bridges across the entire spread are shown in Fig. 2b (see Extended Data Fig. 1 for a set of data without shift in the vertical axis). Near the lower x end (approximately 0.11), LCCO shows superconductivity with the highest $T_c \approx 24$ K (the bottom curve). Here T_c is defined as the temperature at which the superconducting transition commences, as illustrated in Extended Data Fig. 2. Determining T_c using different criteria does not influence any of our analysis (Extended Data Fig. 3). With increasing doping level, T_c gradually decreases, and eventually bridges with higher Ce concentration only show the metallic behaviour, in which the resistivity decreases with decreasing temperature without any abrupt drop of resistance down to the lowest measured temperature of 2 K. The critical composition at which the superconductivity disappears corresponds to the doping level of $x_c \approx 0.177$, which is consistent with previous results[9,16]. For $x > x_c$, the low-temperature dependence of resistivity obeys the Fermi liquid behaviour, namely $\rho = \rho_0 + A_2T^2$ (Fig. 2d), and the T^2 dependence persists to higher temperatures with increasing Ce content, which is highly consistent with previous results[9]. In this study, we focus on the strange-metal state in the superconducting regime, namely the red area in Fig. 2c with $x < x_c$, where the normal-state resistivity shows the linear-in-T behaviour at low temperatures, which is ubiquitous in copper oxide superconductors. With the superconductivity suppressed by magnetic fields (applied perpendicular to the film), the linear-in-T region extends down to the lowest measured temperature, at which the experimental data can be fitted well by $\rho = \rho_0 + A_1T$ (Fig. 2e and Extended Data Fig. 4). In the short-range AF regime (doping below the Fermi surface reconstruction point, $x_{FS} = 0.14$; see Extended Data Fig. 6 for the doping dependence of the Hall coefficient measured on an LCCO composition-spread film), a much higher magnetic field is required to restore the linear-in-T resistivity behaviour (see the high field data for $x = 0.10$ in Extended Data Fig. 5). Similar behaviour for $x = 0.12$ and $x = 0.13$ has also been reported recently[13].

Figure 3a (bottom panel) shows the doping dependence of T_c for the LCCO composition-spread films. Compared with the limited data points obtained from samples made by the traditional synthesis method (light blue squares, extracted from ref. [9]), a clear trend emerges in the dense data from the present combinatorial technique: the dashed line outlining the boundary of the superconducting phase obeys the square root relation $T_c \propto (x_c - x)^{0.5}$ (see Extended Data Fig. 7 for analysis on other systems extracted from the literature). Such a relation is consistent with theoretical predictions for an interaction-driven quantum transition from superconductor to normal metal in the overdoped limit, which has previously been proposed to fit the data of the hole-doped superconductor LSCO in the overdoped region[17]. Here we are able to clearly discern it for the electron-doped LCCO in the overdoped superconducting regime.

Now we turn to the strange-metal state in LCCO. We have extracted the T-linear coefficient A_1 from the 100 μm bridge curves shown here in the top panel of Fig. 3a as a function of the continuous doping level. As introduced by Legros et al.[18], A_1 is normalized by the distance between adjacent CuO_2 planes, that is $A_1^{\square} = A_1/d$, and an unmistakable linear dependence of $A_1^{\square}$ on doping (x) emerges as a result. We note that, before this work, the relation between A_1 and x had, to our knowledge, not been unambiguously quantified owing to serious scattering of data points[10,19]. Without the combinatorial approach, it is difficult to obtain such accurate and systematic data. The newly unearthed relations in turn then immediately point to the square root dependence of T_c on $A_1^{\square}$: Fig. 3b shows T_c versus $(A_1^{\square})^{0.5}$ with the dashed line given by the linear fit $(A_1^{\square})^{0.5} = \alpha T_c + \beta$, with $\alpha = 0.10$ (Ω K^{-1})$^{0.5}$ K^{-1} and $\beta = 1.22$ (Ω K^{-1})$^{0.5}$. Hence, a linear relation between $(A_1^{\square})^{0.5}$ and T_c is established in LCCO.

This relation enables us to make quantitative comparison with other unconventional superconductors. For the typical hole-doped copper

oxide LSCO, the $A_1^{\square}$ versus T_c relation is extracted from the $\rho(T)$ curves of a comprehensive study by Božović et al.[20]. As shown in Fig. 3c, $A_1^{\square}$ shows a similar dependence on T_c. Other than in copper oxides, the relation between $A_1^{\square}$ and T_c has also been observed in the single-band organic superconductor $(TMTSF)_2PF_6$ as well as in the iron-based superconductor $Ba(Fe_{1-x}Co_x)_2As_2$. As summarized in Fig. 3c, there is a single scaling relation that captures the common behaviour among disparate unconventional superconductors, suggestive of a common underlying excitation governing both the strange-metal behaviour and unconventional superconductivity.

The scaling relation observed here can place explicit constraints on theoretical models of linear-in-T resistivity and unconventional superconductivity. Various theoretical scenarios[4,12,21–24] have been proposed to explain the linear-in-T resistivity in copper oxides to date. One conjecture attracting much attention involves the Planckian dissipation[18,24], in which the scattering rate is set by the fundamental Planckian limit given $\hbar/\tau = \alpha k_B T$, irrespective of the underlying scattering mechanisms. Here α is a number close to unity according to previous studies[18,25,26]; $\hbar$, k_B and τ are the reduced Planck constant, Boltzmann constant and relaxation time, respectively. The scaling relation between $A_1^{\square}$ and T_c signals an explicit connection between the normal and superconducting states: whatever the scattering mechanism in the normal state is, it is intimately linked to superconductivity. Even though the Planckian dissipation seems to provide a reasonable description for the linear-in-T resistivity in hole-doped copper oxides from high temperatures down to the lowest measured temperature of 2 K (ref. [18]), in the case of electron-doped copper oxides, the Planckian limit only sets in at low temperatures; at higher temperatures the resistivity of LCCO evolves into a power-law dependence that exceeds the extrapolation of the perfect linear-in-T resistivity (Extended Data Fig. 8). This deviation observed in the electron-doped copper oxides has been also pointed out in ref. [11]. In fact, our finding of a linear relation between $A_1^{\square}$ and x is clearly different from the Planckian estimate[18], where non-linear $A_1^{\square}(x)$ curves were extracted for both the electron- and hole-doped copper oxides based on $A_1^{\square} \propto 1/T_F \propto m^*/n$. Here T_F is the Fermi temperature, m^* is the effective mass obtained from quantum oscillations and specific heat measurements, and n is the carrier density calculated using the Luttinger rule $n = (1-x)/(a^2 d)$, where a is the in-plane lattice constant and d is the distance between adjacent CuO_2 planes.

Alternatively, the linear-in-T resistivity as well as electron pairing could directly stem from the AF spin fluctuations associated with quantum criticality[3,23,27,28]. This picture is best substantiated in $(TMTSF)_2PF_6$, in which superconductivity is intimately tied to the spin density wave fluctuations and a perfect linear-in-T resistivity is observed as T approaches zero[10,29–31]. Very similar transport properties and evolution of ground states in the phase diagrams between LCCO and $(TMTSF)_2PF_6$ may be an indication that AF spin fluctuations are also at work in electron-doped copper oxides. Recalling that $T_c \propto (x_c - x)^{0.5}$ is consistent with an interaction-driven quantum transition from superconductor to normal metal in the overdoped limit[17], that is, change of pairing energy plays the primary role in controlling T_c, we argue that AF spin fluctuations involved in electron correlations are responsible for both the superconductivity and the strange-metal behaviour in the normal state. This picture is also in line with the fact that perfect linear-in-T resistivity appears in proximity to the temperature and the doping region where short-range AF orders (fluctuations) are present[9,11]. Analogous behaviour has also been seen in the iron-based superconductor $Ba(Fe_{1-x}Co_x)_2As_2$ (ref. [32]). Although the situation is more complex in hole-doped copper oxides involving pseudogap and intertwined orders[33], the single scaling relation observed here might be the common signature of the interplay among linear-in-T resistivity, pairing correlations and spin fluctuations[10,31]. A microscopic description of how the pairing is mediated by spin fluctuations remains an open question but, given the common behaviour observed across different families of superconductors, renewed and focused theoretical investigations are perhaps in order.

We note that, in an earlier study of electron irradiation on a hole-doped cuprate $YBa_2CuO_{7-\delta}$ (ref. [34]), a varying amount of disorder was found to affect T_c substantially, but the slope of the linear-in-T resistivity barely changed, which seemingly disagrees with the scaling law reported here. However, different from the systematic chemical substitution in our study, electron irradiation introduces Cu and O vacancies in the CuO_2 planes, which can alter the local Cu-O electronic structure[35]. Therefore, we do not expect the scaling law observed in pure compounds to apply to such disordered materials.

In Fig. 3b, the linear fit of $(A_1^{\square})^{0.5}$ extrapolates to a finite value at $T_c = 0$, which is also visible in $Bi_2Sr_2CuO_{6+\delta}$ and LSCO[19,36]. However, approaching the QCP at the end of the superconducting dome where $T_c = 0$, the linear-in-T resistivity disappears, that is $A_1^{\square}$ becomes zero[9]. This deviation is possibly due to quantum fluctuations or strong pairing fluctuations[37] near QCP, leading to the deviation of $(A_1^{\square})^{0.5}$ from the linear dependence. Unfortunately, the uncertainty in the determination of T_c and the reduced temperature range for linear-in-T resistivity close to QCP prevent us from obtaining a quantitative picture in this region. Further investigations are ongoing in search of further insight into the origin of superconductivity in the overdoped side of LCCO.

Online content

Any methods, additional references, Nature Research reporting summaries, source data, extended data, supplementary information, acknowledgements, peer review information; details of author contributions and competing interests; and statements of data and code availability are available at https://doi.org/10.1038/s41586-021-04305-5.

1. Lee, P. A., Nagaosa, N. & Wen, X.-G. Doping a Mott insulator: physics of high-temperature superconductivity. *Rev. Mod. Phys.* **78**, 17–85 (2006).
2. Armitage, N. P., Fournier, P. & Greene, R. L. Progress and perspectives on electron-doped cuprates. *Rev. Mod. Phys.* **82**, 2421–2487 (2010).
3. Scalapino, D. J. A common thread: the pairing interaction for unconventional superconductors. *Rev. Mod. Phys.* **84**, 1383–1417 (2012).
4. Keimer, B., Kivelson, S. A., Norman, M. R., Uchida, S. & Zaanen, J. From quantum matter to high-temperature superconductivity in copper oxides. *Nature* **518**, 179–186 (2015).
5. Gurvitch, M. & Fiory, A. T. Resistivity of $La_{1.825}Sr_{0.175}CuO_4$ and $YBa_2Cu_3O_7$ to 1100 K: absence of saturation and its implications. *Phys. Rev. Lett.* **59**, 1337–1340 (1987).
6. Takagi, H. et al. Systematic evolution of temperature-dependent resistivity in $La_{2-x}Sr_xCuO_4$. *Phys. Rev. Lett.* **69**, 2975–2978 (1992).
7. Cooper, R. A. et al. Anomalous criticality in the electrical resistivity of $La_{2-x}Sr_xCuO_4$. *Science* **323**, 603–607 (2009).
8. Fournier, P. et al. Insulator-metal crossover near optimal doping in $Pr_{2-x}Ce_xCuO_4$: anomalous normal-state low temperature resistivity. *Phys. Rev. Lett.* **81**, 4720–4723 (1998).
9. Jin, K., Butch, N. P., Kirshenbaum, K., Paglione, J. & Greene, R. L. Link between spin fluctuations and electron pairing in copper oxide superconductors. *Nature* **476**, 73–75 (2011).
10. Taillefer, L. Scattering and pairing in cuprate superconductors. *Annu. Rev. Condens. Matter Phys.* **1**, 51–70 (2010).
11. Greene, R. L., Mandal, P. R., Poniatowski, N. R. & Sarkar, T. The strange metal state of the electron-doped cuprates. *Annu. Rev. Condens. Matter Phys.* **11**, 213–229 (2020).
12. Varma, C. M. Colloquium: linear in temperature resistivity and associated mysteries including high temperature superconductivity. *Rev. Mod. Phys.* **92**, 031001 (2020).
13. Sarkar, T. et al. Hidden strange metallic state in underdoped electron-doped cuprates. *Phys. Rev. B* **103**, 224501 (2021).
14. Koinuma, H. & Takeuchi, I. Combinatorial solid-state chemistry of inorganic materials. *Nat. Mater.* **3**, 429–438 (2004).
15. Yuan, J., Stanev, V., Gao, C., Takeuchi, I. & Jin, K. Recent advances in high-throughput superconductivity research. *Supercond. Sci. Technol.* **32**, 123001 (2019).
16. Sarkar, T. et al. Ferromagnetic order beyond the superconducting dome in a cuprate superconductor. *Science* **368**, 532–534 (2020).
17. Schneider, T. & Singer, J. M. *Phase Transition Approach to High Temperature Superconductivity* (Imperial College Press, 2000).
18. Legros, A. et al. Universal T-linear resistivity and Planckian dissipation in overdoped cuprates. *Nat. Phys.* **15**, 142–147 (2019).
19. Ayres, J. et al. Incoherent transport across the strange-metal regime of overdoped cuprates. *Nature* **595**, 661–666 (2021).
20. Božović, I., He, X., Wu, J. & Bollinger, A. T. Dependence of the critical temperature in overdoped copper oxides on superfluid density. *Nature* **536**, 309–311 (2016).
21. Anderson, P. W. The resonating valence bond state in La_2CuO_4 and superconductivity. *Sci. New Ser.* **235**, 1196–1198 (1987).

22. Varma, C. M., Littlewood, P. B., Schmitt-Rink, S., Abrahams, E. & Ruckenstein, A. E. Phenomenology of the normal state of Cu-O high-temperature superconductors. *Phys. Rev. Lett.* **63**, 1996–1999 (1989).
23. Sachdev, S. Quantum phase transitions. *Phys. World* **12**, 33–38 (1999).
24. Zaanen, J. Why the temperature is high. *Nature* **430**, 512–513 (2004).
25. Bruin, J. a. N., Sakai, H., Perry, R. S. & Mackenzie, A. P. Similarity of scattering rates in metals showing T-linear resistivity. *Science* **339**, 804–807 (2013).
26. Licciardello, S. et al. Electrical resistivity across a nematic quantum critical point. *Nature* **567**, 213–217 (2019).
27. Moriya, T. & Ueda, K. Spin fluctuations and high temperature superconductivity. *Adv. Phys.* **49**, 555–606 (2000).
28. Monthoux, P. & Pines, D. Spin-fluctuation-induced superconductivity and normal-state properties of $YBa_2Cu_3O_7$. *Phys. Rev. B* **49**, 4261–4278 (1994).
29. Bourbonnais, C. & Sedeki, A. Link between antiferromagnetism and superconductivity probed by nuclear spin relaxation in organic conductors. *Phys. Rev. B* **80**, 085105 (2009).
30. Doiron-Leyraud, N. et al. Correlation between linear resistivity and T_c in the Bechgaard salts and the pnictide superconductor $Ba(Fe_{1-x}Co_x)_2As_2$. *Phys. Rev. B* **80**, 214531 (2009).
31. Sedeki, A., Bergeron, D. & Bourbonnais, C. Extended quantum criticality of low-dimensional superconductors near a spin-density-wave instability. *Phys. Rev. B* **85**, 165129 (2012).
32. Fang, L. et al. Roles of multiband effects and electron-hole asymmetry in the superconductivity and normal-state properties of $Ba(Fe_{1-x}Co_x)_2As_2$. *Phys. Rev. B* **80**, 140508 (2009).
33. Fradkin, E., Kivelson, S. A. & Tranquada, J. M. Colloquium: theory of intertwined orders in high temperature superconductors. *Rev. Mod. Phys.* **87**, 457–482 (2015).
34. Rullier-Albenque, F., Alloul, H. & Tourbot, R. Influence of pair breaking and phase fluctuations on disordered high T_c cuprate superconductors. *Phys. Rev. Lett.* **91**, 047001 (2003).
35. Emery, V. J. & Kivelson, S. A. Superconductivity in bad metals. *Phys. Rev. Lett.* **74**, 3253–3256 (1995).
36. Hussey, N. E., Gordon-Moys, H., Kokalj, J. & McKenzie, R. H. Generic strange-metal behaviour of overdoped cuprates. *J. Phys. Conf. Ser.* **449**, 012004 (2013).
37. Maier, T. A., Karakuzu, S. & Scalapino, D. J. Overdoped end of the cuprate phase diagram. *Phys. Rev. Res.* **2**, 033132 (2020).

Methods

Film growth

We fabricated $La_{2-x}Ce_xCuO_4$ (x = 0.10–0.19) composition-spread thin films on STO substrates (10×10 mm^2 in size) with a programmable moving shadow mask. Two targets with compositions $La_{1.9}Ce_{0.1}CuO_4$ (that is, x = 0.10) and $La_{1.81}Ce_{0.19}CuO_4$ (that is, x = 0.19) were ablated alternately by excimer KrF laser pulses (wavelength λ = 248 nm). During the deposition, a moving mask with constant speed was used to generate opposing thickness wedges from the two targets. The deposition rates were carefully controlled to ensure that the film deposited in one pair of wedge depositions never exceeded a single-cell layer to avoid the formation of superlattices. With 80 periods, a 100-nm-thick combinatorial LCCO film was fabricated followed by an in situ reduction process of several minutes in vacuum at about 700 °C.

Structural characterization

The crystallinity of the entire film was first characterized by an in-house X-ray diffractometer. The beam spot size was 0.4 mm in width, which was regulated by a slit, and it was set to examine the spread film from one end to the other along the doping gradient direction, with 2θ scanning in the range of 10° to 80° at each spot. The spread film was also examined by synchrotron microdiffraction at Advanced Light Source (Beamline 12.3.2) with a beam spot of 1 μm^2. The sampling interval was 10 μm along the doping gradient direction (horizontal), and several points were also measured at each horizontal position with a vertical direction interval of 20 μm.

Transport measurements

The composition-spread thin films were patterned into small bridges, to measure electrical resistivity from 300 K to low temperatures. There were three levels of device array patterns with successively smaller microbridge widths, and each set of measurements was followed by patterning and measurements from the next level. In this manner, the highest spatial resolution of the transport measurement was on the scale of 20 μm, which is comparable to the micrometre resolution of synchrotron structural characterization.

Electrical contacts were made by indium soldering or wire bonding. The sample resistance was measured with a standard four-terminal geometry. The temperature dependence of resistivity was measured using commercial cryostations. For Hall measurements, the sample was patterned into a standard Hall-bar geometry.

Evolution of the Hall coefficient with doping

For a Ce concentration around optimal doping (Extended Data Fig. 6a, $x \approx 0.117$), the Hall resistivity ρ_{xy} exhibits a complex behaviour, that is, it is negative at high temperatures, changes to positive at an intermediate temperature range (20–50 K) and then becomes negative again at lower temperatures. For Ce concentrations above 0.14 (Extended Data Fig. 6c–e), ρ_{xy} remains positive in the whole measuring temperature range (2–100 K). The ρ_{xy} versus magnetic field B curves for different Ce concentrations (Extended Data Fig. 6f) underline the evolution at low temperatures (T = 2 K). Extended Data Figure 6g shows the temperature dependence of the Hall coefficient R_H ($=\rho_{xy}/B$) measured at B = 14 T. With Ce doping in the range of $0.11 < x < 0.14$, the temperature dependence of R_H exhibits a broad peak at approximately 20 K. This peak is gradually suppressed with increasing Ce concentration and evolves into a plateau at low temperatures for $x > 0.14$. This behaviour offers valuable information about the evolution of Fermi surface, and Extended Data Fig. 6h, i gives a more intuitive picture of this evolution. In the Ce doping dependence of R_H (B = 14 T and T = 2 K, Extended Data Fig. 6h), with Ce concentration increasing from 0.11 to around 0.14, R_H increases rapidly with its sign changing from negative to positive. At a higher Ce concentration, R_H exhibits a gentle and smooth decrease as a function of x. Extended Data Figure 6i shows the corresponding doping dependence of Hall number n_H ($= V/eR_H$), where V is the volume per copper and e is the charge of the carrier. To summarize, with the increase of Ce doping, R_H (n_H) shows a marked change in the range of $0.11 < x < 0.14$ and becomes less sensitive to x thereafter. Overall, this behaviour is highly consistent with previous studies obtained on uniform LCCO films with different Ce concentrations[9,38–41]. The peaking behaviour in the temperature dependence of R_H is associated with the Fermi surface reconstruction induced by an AF order at low temperatures[9,41]. The Fermi surface reconstruction at $x \approx 0.14$ corresponds to the disappearance of the peak behaviour in the R_H versus T plot (Extended Data Fig. 6g) and the plateau at $x > 0.14$ in the R_H versus x plot (Extended Data Fig. 6h). The Hall number n_H versus x plot (Extended Data Fig. 6i) is also consistent with the previous study[41]. Therefore, the Hall signals obtained here closely reflect the known evolution of Fermiology as a function of Ce concentration. Note that our measurements were performed on a single combinatorial LCCO film, over just a week, and yet the results capture the most salient characteristics of the band structure evolution in LCCO as a function of Ce doping previously amassed over decades, demonstrating the advantage and effectiveness of our thin-film composition-spread approach.

Data availability

The data that support the findings of this study are available in the paper. Additional data are available from the corresponding authors upon reasonable request.

38. Zhang, X. et al. Quantum criticality tuned by magnetic field in optimally electron-doped cuprate thin films. *Phys. Rev. B* **103**, 014517 (2021).
39. Jin, K., Zhu, B. Y., Wu, B. X., Gao, L. J. & Zhao, B. R. Low-temperature Hall effect in electron-doped superconducting $La_{2-x}Ce_xCuO_4$ thin films. *Phys. Rev. B* **78**, 174521 (2008).
40. Jin, K., Zhang, X. H., Bach, P. & Greene, R. L. Evidence for antiferromagnetic order in $La_{2-x}Ce_xCuO_4$ from angular magnetoresistance measurements. *Phys. Rev. B* **80**, 012501 (2009).
41. Sarkar, T. et al. Fermi surface reconstruction and anomalous low-temperature resistivity in electron-doped $La_{2-x}Ce_xCuO_4$. *Phys. Rev. B* **96**, 155449 (2017).
42. Ando, Y., Komiya, S., Segawa, K., Ono, S. & Kurita, Y. Electronic phase diagram of high-T_c cuprate superconductors from a mapping of the in-plane resistivity curvature. *Phys. Rev. Lett.* **93**, 267001 (2004).

Acknowledgements We thank R. Greene for many fruitful discussions and inspiring comments during the preparation of the manuscript. We thank T. Schneider for discussions surrounding the scaling relations. We thank G. Zhang, Z. Weng, Y. Li, Y. Zhou and E. Liu for fruitful discussions. We thank S. Tu and Y. Zou for experimental assistance. This work was supported by the National Key Basic Research Program of China (grant nos. 2017YFA0302900, 2017YFA0303003 and 2018YFB0704102), the National Natural Science Foundation of China (grant nos. 11888101, 11927808, 11834016 and 11961141008), Beijing Natural Science Foundation (grant no. Z190008), the Strategic Priority Research Program (B) of Chinese Academy of Sciences (grant nos. XDB25000000 and XDB33000000), the CAS Interdisciplinary Innovation Team, Key-Area Research and Development Program of Guangdong Province (grant no. 2020B0101340002). The work at the University of Maryland was supported by grant nos. AFOSR FA9550-14-10332, AFOSR FA9550-22-10023, ONR N00014-13-1-0635 and ONR N00014-15-2-222, and NIST grant no. 60NANB19D027. This research used BL12.3.2 of the Advanced Light Source, a US Department of Energy Office of Science User Facility under contract no. DE-AC02-05CH11231.

Author contributions K. Jin conceived the project. K. Jin, J.Y. and Q.C. supervised the experiments. Z.F., Z.L. and H.Y. synthesized the composition-spread films. G.H., J.Z., X.Z. and M.Q. performed the transport measurements. N.T. and I.T. carried out the synchrotron XRD measurements. X.J., Y.S., Y.Z., Z.G.C., I.T., J.Y., Q.C., K. Jin and Z.Z. analysed the experimental data. K. Jiang, Y.-f.Y., T.X. and J.H. provided theoretical understanding. Q.C, J.Y., I.T. and K. Jin wrote the manuscript with input from all authors.

Competing interests The authors declare no competing interests.

Additional information
Correspondence and requests for materials should be addressed to Jiangping Hu, Ichiro Takeuchi or Kui Jin.

Peer review information *Nature* thanks the anonymous reviewers for their contribution to the peer review of this work.

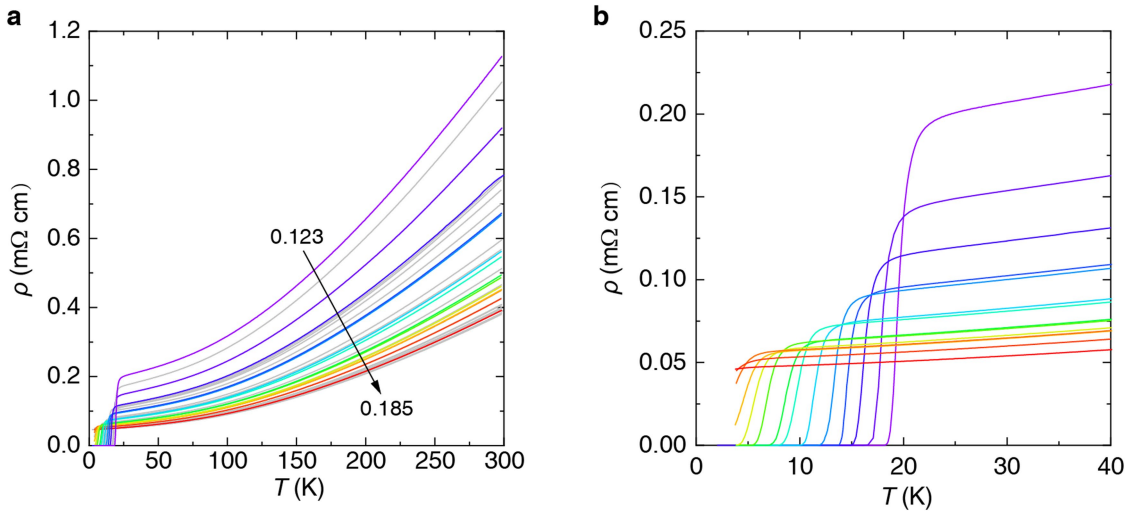

Extended Data Fig. 1 | Temperature dependence of resistivity for different bridges (100-μm width) across a combinatorial $La_{2-x}Ce_xCuO_4$ (LCCO) film. **a**, The doping varies from 0.123 to 0.185 from the top to the bottom, as indicated by the arrow. These curves provide the raw data for extracting the $A_1^{\square}$ vs. x, and $A_1^{\square}$ vs. T_c dependences shown in Figs. 3a and 3b of the main text. **b**, The low-temperature range of the colored lines in panel **a**. The doping for each curve is (normal-state resistivity from top to bottom): 0.123, 0.129, 0.138, 0.144, 0.148, 0.152, 0.156, 0.160, 0.162, 0.165, 0.167, 0.168, 0.169, and 0.175.

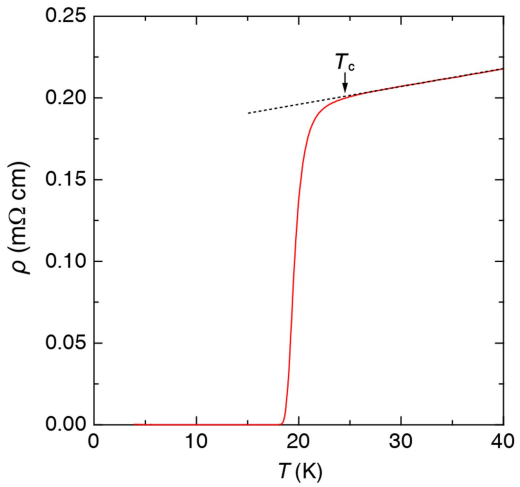

Extended Data Fig. 2 | Definition of T_c in the main text. The solid red curve is a typical $\rho(T)$ curve of a 100-μm bridge from the combinatorial $La_{2-x}Ce_xCuO_4$ (LCCO) film. The black dashed line is a linear extension of the normal-state resistivity to lower temperatures. The arrow indicates where the resistivity starts to deviate from the linear extension, which is defined as T_c in this work.

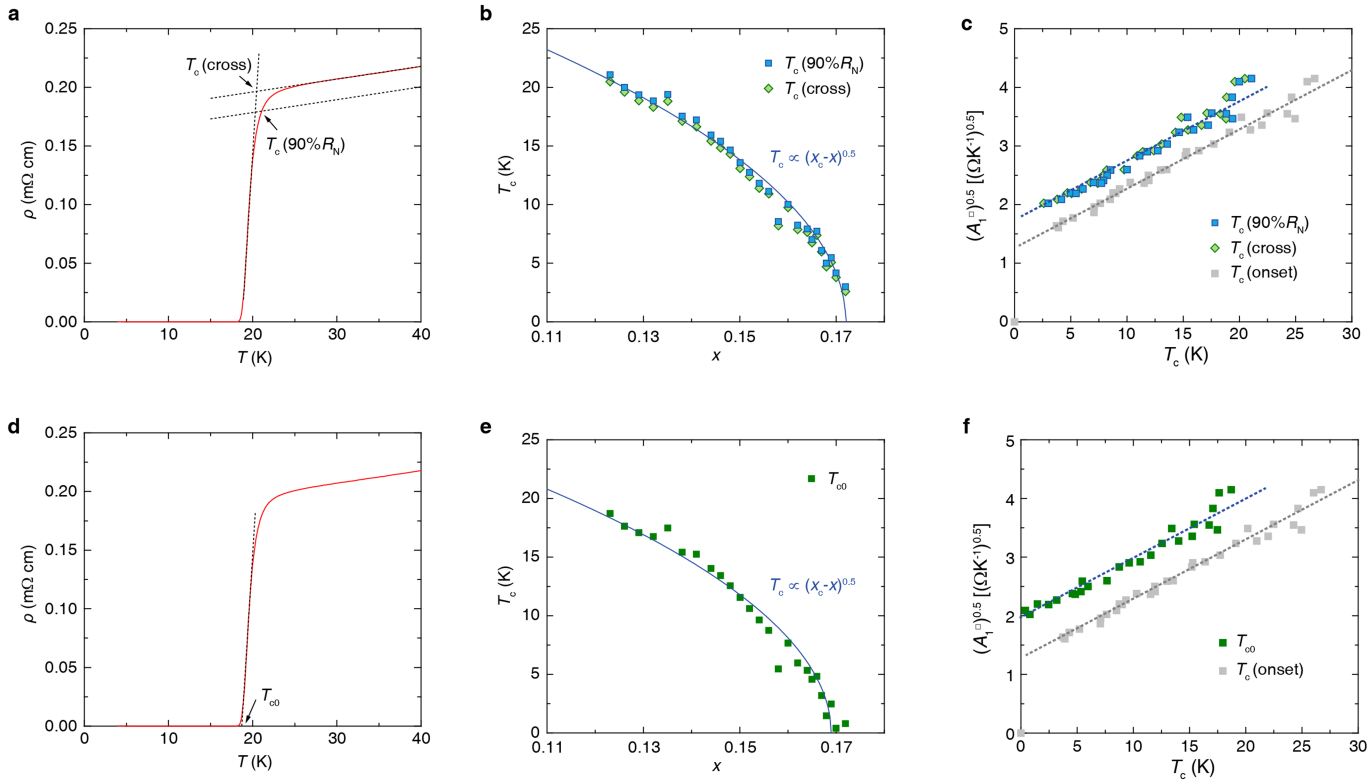

Extended Data Fig. 3 | Comparison of different T_c definitions. a, T_c(cross) is defined as the temperature where the linear extrapolation crosses extrapolation of the bulk of the resistance drop due to superconducting transition. T_c(90%R_N) is defined as the temperature where the resistivity is 90% of the normal-state resistivity. The lower dashed line is obtained by maintaining the slope of the linear extrapolation of the normal-state resistivity, while multiplying the intercept by 0.9. **b**, T_c as a function of doping. The solid line shows the fit with the formula: $T_c \propto (x_c - x)^{0.5}$. **c**, Comparison of the scaling relation between $(A_1^{\square})^{0.5}$ and different definitions of T_c. **d**, T_{c0} is extracted by extrapolating the bulk of the resistance drop to zero resistivity. **e**, T_c as a function of doping. The solid line shows the fit with the formula: $T_c \propto (x_c - x)^{0.5}$. **f**, Comparison of the scaling relation between $(A_1^{\square})^{0.5}$ vs. T_c(onset) and $(A_1^{\square})^{0.5}$ vs. T_{c0}. Although there are a few kelvins difference between different definitions of T_c, the parabolic relation between T_c and x and linear scaling relation between $(A_1^{\square})^{0.5}$ and T_c are valid in all three.

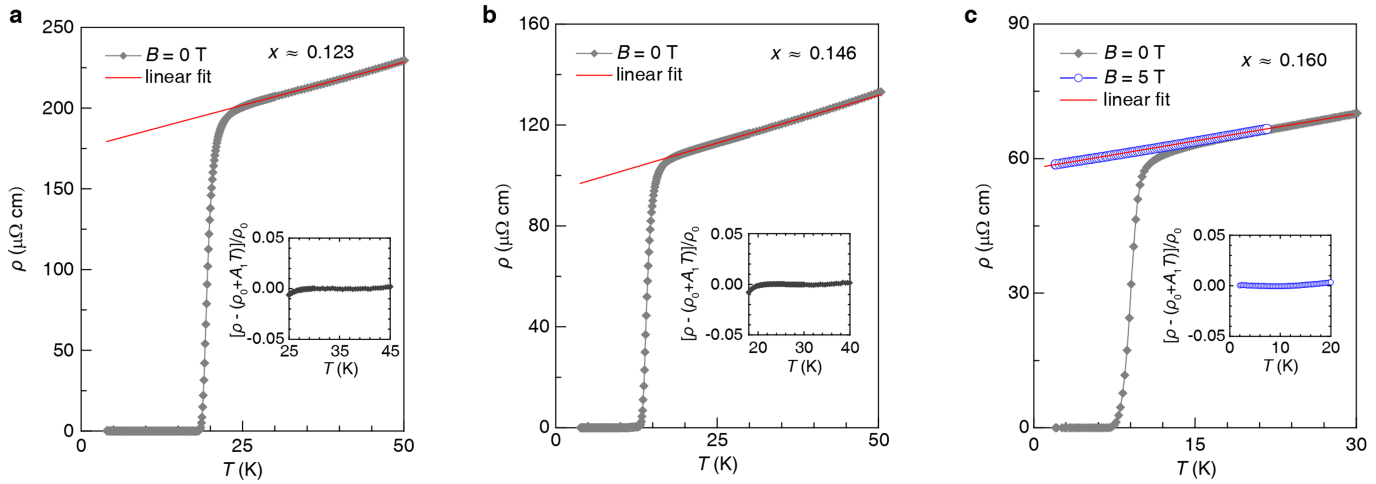

Extended Data Fig. 4 | Linear-in-*T* resistivity in superconducting LCCO. **a**–**b**, Temperature dependence of resistivity $\rho(T)$ in zero field (diamonds), fitted by $\rho(T) = \rho_0 + A_1 T$ (red line), for $x \approx 0.123$ (**a**) and 0.146 (**b**). **c**, $\rho(T)$ of $x \approx 0.160$ at $B = 0$ (grey diamonds) and $B = 5$ T (blue circles). The red line is the linear fit to the 5 T data. The insets show the fitting quality presented as $\Delta\rho/\rho_0$ vs. T, where $\Delta\rho = \rho - (\rho_0 + A_1 T)$.

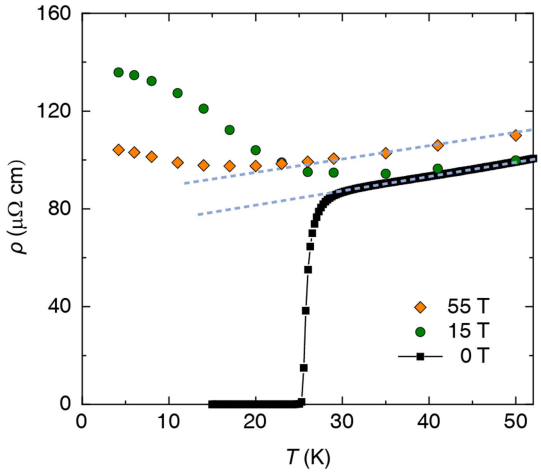

Extended Data Fig. 5 | Temperature dependence of resistivity for the LCCO film around optimal doping ($x = 0.10$). Magnetic fields are applied along the *c*-axis direction of the LCCO film: 0 T (black squares), 15 T (green circles) and 55 T (orange diamonds). The linear-in-*T* resistivity is gradually recovered at high magnetic fields. Dashed lines mark the linear-in-*T* resistivity region at $B = 0$ and 55 T. Data adapted from ref. [38].

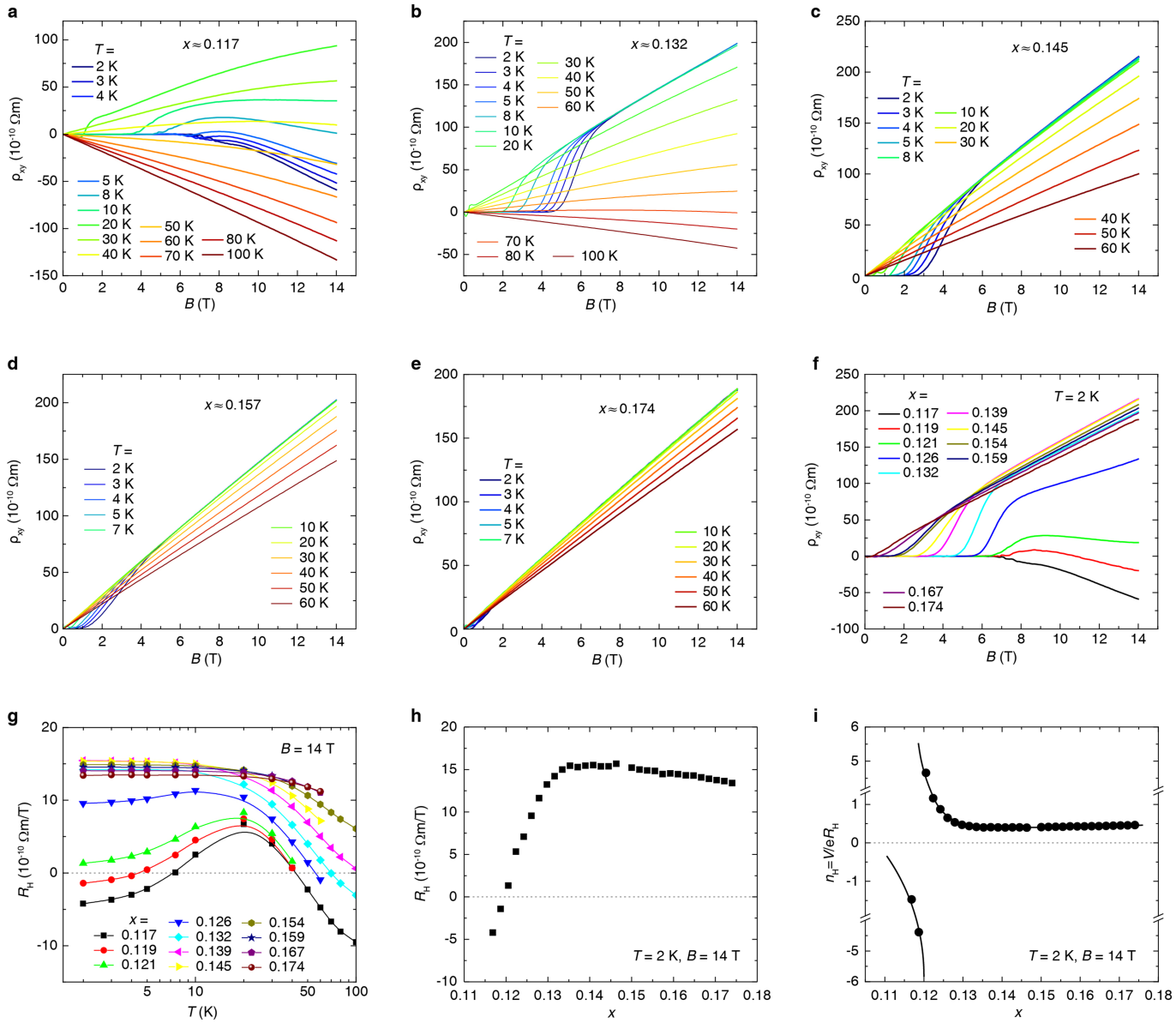

Extended Data Fig. 6 | Evolution of Hall signal as a function of doping measured on a combinatorial film. a–**e**, The Hall resistivity (ρ_{xy}) as a function of magnetic field (applied perpendicular to the *ab*-plane of the LCCO film) at different temperatures, for Ce doping $x \approx 0.117$ (**a**), 0.132 (**b**), 0.145 (**c**), 0.157 (**d**), and 0.174 (**e**). **f**, ρ_{xy} vs. B at $T = 2$ K for different Ce concentrations from 0.117 to 0.174. **g**, Temperature dependence of the Hall coefficient (R_H) for different Ce concentrations from 0.117 to 0.174, measured at a magnetic field of 14 T. **h**, R_H at $T = 2$ K and $B = 14$ T as a function of Ce doping. **i**, The corresponding Ce doping dependence of Hall number $n_H = V/eR_H$.

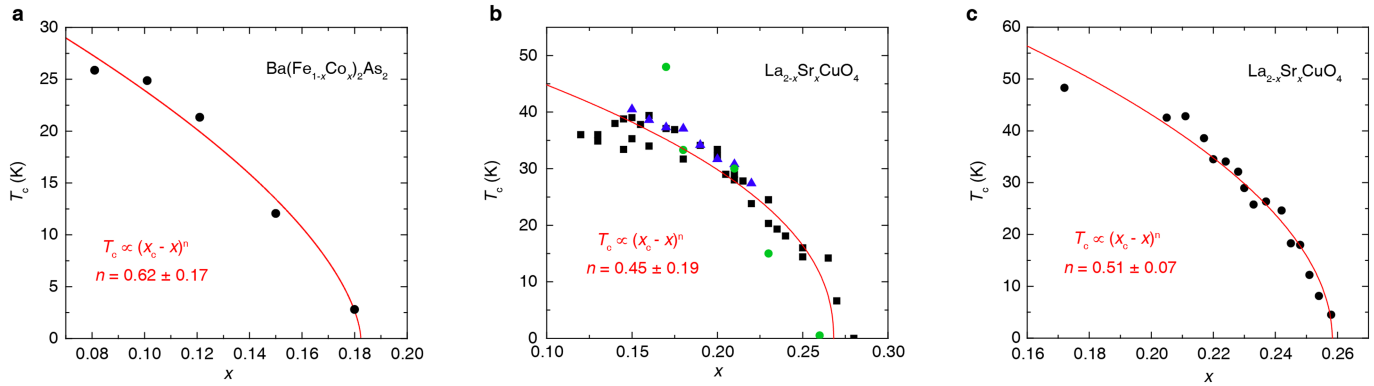

Extended Data Fig. 7 | T_c versus x plots for different unconventional superconductors. Symbols are data extracted from literature and solid curves are fits with the formula $T_c \propto (x_c - x)^n$, with n being a fitting parameter. **a**, Data for $Ba(Fe_{1-x}Co_x)_2As_2$ extracted from ref. [10]. **b**, Data for $La_{2-x}Sr_xCuO_4$ (black squares: ref. [17]; green dots: ref. [7]; blue triangles: ref. [42]). **c**, Data for $La_{2-x}Sr_xCuO_4$ extracted from the $\rho(T)$ curves of ref. [20]. The exponent n for different materials fall in the range of 0.4–0.6. For $Ba(Fe_{1-x}Co_x)_2As_2$, the data is scarce and the fitting uncertainty is relatively large. $La_{2-x}Sr_xCuO_4$ is one of the most intensively studied hole-doped copper oxide, thus there are more data in literature. However, data from different studies (panel **b**) are quite scattered thus the fit is poor. In panel **c**, the data are extracted from a relatively comprehensive study of $La_{2-x}Sr_xCuO_4$ (ref. [20]), which is in a relatively good fit to the formula $T_c \propto (x_c - x)^n$ with $n = 0.51 \pm 0.07$, consistent with the value reported in this work, and the uncertainty is smaller compared to the other two panels.

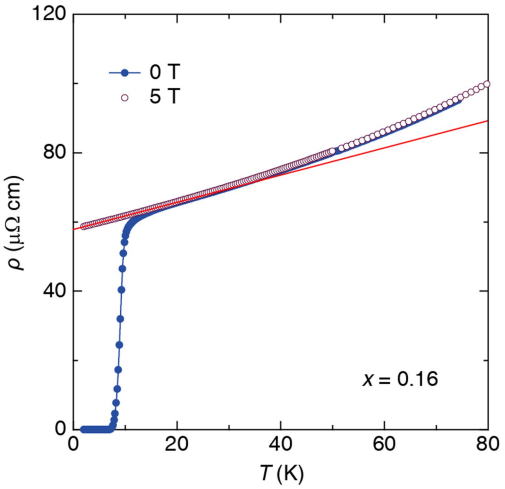

Extended Data Fig. 8 | Temperature dependence of the resistivity for a bridge with T_c ~ 10 K (x = 0.16) at B = 0 T and B = 5 T. The red straight line indicates the extrapolation of the low-temperature linear fit to higher temperatures.

Extended Data Table 1 | Doping, *c*-axis, T_c and linear-in-T coefficients for the data shown in Fig. 3 of the main text

x	T_c (K)	c-axis (Å)	$A_1^{\square}$ (Ω/K)	$\sqrt{A_1^{\square}}$ $[(\Omega/\mathrm{K})^{0.5}]$
0.123	26.7	12.427	17.21	4.15
0.126	26.03	12.424	16.79	4.10
0.129	24.65	12.421	14.67	3.83
0.132	24.26	12.418	12.59	3.55
0.135	24.95	12.415	12.00	3.46
0.138	22.48	12.413	12.67	3.56
0.141	22	12.41	11.25	3.35
0.144	20.98	12.408	10.72	3.27
0.146	20.18	12.406	12.17	3.49
0.148	19.12	12.405	10.46	3.23
0.150	17.72	12.404	9.20	3.03
0.152	16.39	12.403	8.53	2.92
0.154	15.29	12.401	8.42	2.90
0.156	15.2	12.4	8.03	2.83
0.158	13	12.399	6.71	2.59
0.160	13.54	12.398	6.74	2.60
0.162	11.91	12.396	6.25	2.50
0.164	11.94	12.395	5.82	2.41
0.165	10.29	12.395	5.66	2.38
0.166	11.53	12.394	5.59	2.37
0.167	9.35	12.394	5.14	2.27
0.168	8.76	12.393	4.84	2.20
0.169	9	12.392	4.80	2.19
0.170	8.51	12.391	4.37	2.09
0.172	7.63	12.39	4.09	2.02
0.173	7.09	12.39	3.84	1.96
0.175	7.07	12.388	3.47	1.86
0.176	5.21	12.388	3.14	1.77
0.177	4.3	12.388	2.94	1.71
0.178	3.73	12.387	2.68	1.64
0.179	3.9	12.387	2.58	1.61